Reverse-neural network assisted analysis of of Autler-Townes doublet in the trap-loss fluorescence spectroscopy of cesium MOT with single step Rydberg excitation

Xiaokai Hou[1], Yuewei Wang[1], Jun He[1,2], and Junmin Wang[1,2,*]

[1]State Key Laboratory of Quantum Optics Technologies and Devices, and Institute of Opto-Electronics, Shanxi University, Tai Yuan 030006, Shanxi Province, China
[2]Collaborative Innovation Center of Extreme Optics, Shanxi University, Tai Yuan 030006, Shanxi Province, China
[*]Corresponding, wwjjmm@sxu.edu.cn

ABSTRACT

Autler-Townes (AT) doublet, a fundamental manifestation of quantum interference effects, serves as a critical tool for studying the dynamic behavior of Rydberg atoms. However, the limited availability of experimental data in cold atom system and the inherent complexity of nonlinear behaviors present substantial challenges for precise analysis of AT doublet's characteristics. Here, we introduce innovatively a reverse neural network (RNN) to investigate AT doublet of the trap-loss fluorescence spectroscopy (TLFS) in cesium (Cs) magneto-optical trap (MOT) with single-step Rydberg excitation using a 319-nm ultraviolet (UV) laser. Through a combination of theoretical analysis and experimental data, a model is developed to describe the V-type three-level system with Rydberg state of Cs atoms, elucidating the nonlinear relationship between cooling laser detuning and the AT doublet interval and symmetry. Experimental results indicate that with decreasing cooling laser detuning, the AT doublet exhibits increasing symmetry, whereas the AT doublet interval shows a nonlinear decrease. Utilizing the RNN to generate high-density datasets significantly enhances the resolution and precision of the nonlinear relationship analysis. The experimental data closely align with the theoretical model and RNN predictions, validating the efficacy of the RNN in optimizing experimental parameters and analyzing complex nonlinear physical systems. This work serves as a valuable technical reference for advancing spectroscopic techniques and applying machine learning to nonlinear physical challenges, offering novel tools and perspectives for research in cold atom physics and quantum optics.

Introduction

Rydberg atoms[1], highly-excited atoms with principal quantum numbers n > 10, have shown great promise in terms of their unique structure. These physical properties scale with principal quantum number n, such as long radiation lifetime ($\sim n^3$), strong dipole–dipole interaction ($\sim n^4$) and large polarizability ($\sim n^7$). They have found extensive applications in many-body physics[2], quantum information and computing[3,4], precision measurement[5–9]. To exploit coherent quantum dynamics, these experiments are performed on timescales shorter than the lifetime of Rydberg state. However, for the realization of supersolids[10], frustrated quantum magnetism[11] or spin squeezing for enhanced metrology[12], it is necessary to extend the investigation time of Rydberg atoms. To take advantage of the long coherence time of ground state atoms and the strong long-range interaction between Rydberg atoms, we can create a wave function that is mostly ground state with an adjustable Rydberg component by off-resonantly coupling the ground state to Rydberg state[5,13,14], which is called Rydberg dressing approach. Therefore, experimental research of Autler–Townes (AT) doublet[15] has opened a route to produce the dressed-state atoms with the long coherence time and controllable long-range interaction by adjusting the coupling intensity and detuning between the ground state and Rydberg state.

AT doublet, a quintessential manifestation of quantum interference effects, is characterized by key properties such as the interval, symmetry, and the width of the spectral double-peaks structure, all of which are intricately linked to parameters like the Rabi frequency and detuning of the coupling laser field[7,16,17,21]. Consequently, a comprehensive investigation of AT doublet properties is pivotal for elucidating the dynamic mechanisms Rydberg dressing ground state and for uncovering nonlinear effects in complex systems. Nevertheless, the sparsity of experimental data coupled with the nonlinear intricacy of spectral properties presents a formidable challenge in efficiently extracting the characteristic parameters of AT doublet. Traditional interpolation methods often rely on predefined functional profiles and struggle with sparse data or strongly coupled parameters, limiting their effectiveness. In contrast, the reverse neural network (RNN) demonstrates significant advantages in handling

nonlinear processes of unknown functions. With their powerful learning capability, RNN do not require a specific functional form, allowing them to automatically extract hidden nonlinear features from data and establish highly complex mappings between input parameters and output characteristics through training.

Based on the superior flexibility and robustness of RNN in addressing unknown nonlinear systems, we have innovatively introduced an RNN architecture, integrated with advanced machine learning techniques[23,24], to generate high-density experimental datasets, providing a transformative solution to the challenges of spectral analysis due to sparse data. By inversely mapping experimental condition parameters from target outputs, the RNN not only facilitates the generation of high-density experimental datasets but also significantly enhances fitting accuracy and broadens the scope of data analysis capabilities. In recent years, the deployment of machine learning in the physical sciences has witnessed rapid growth, particularly in tackling complex nonlinear problems, where it has demonstrated remarkable potential. Experimental results reveal that the AT doublet progressively converge toward symmetry, while the AT doublet interval exhibits a nonlinear reduction as the cooling laser detuning diminishes. This methodology underscores the significant potential of machine learning in nonlinear data processing within complex physical systems, offering a valuable technical reference for advancing cold atomic physics research and extracting spectral characteristic parameters.

In this paper, we systematically investigate the characteristics of the AT doublet of the trap-loss fluorescence spectroscopy (TLFS) of in cesium (Cs) magneto-optical traps (MOT) using single-step ultraviolet (UV) laser excitation. First, a theoretical model describing the three-level V-type system of Cs atoms is established, analyzing the relationship between cooling laser detuning and AT doublet characteristics. Second, using TLFS, experimental observations of AT doublet under different cooling laser parameters are conducted, confirming that the symmetry of the AT doublet improves as detuning decreases, while the AT doublet interval exhibits a nonlinear reduction trend. Finally, a RNN architecture is employed to address the limitations of sparse experimental data by generating high-density datasets, thereby improving the precision of nonlinear fitting and parameter optimization, and further validating the applicability and stability of this approach in modeling complex physical systems.

The V-type three-level system with Rydberg state of Cs atoms

As depicted in Fig.1, here is a V-type three-level system comprising the Cs ground state $6S_{1/2}$ (F=4) (denoted as $|1\rangle$), the Cs atom excited state $6P_{3/2}$ ($F^{'}=5$) (denoted as $|2\rangle$), and the Cs atom Rydberg state $nP_{3/2}$ (m_J=+3/2) (denoted as $|3\rangle$). Ω_1 denotes the Rabi frequency of the excitation laser (coupling Levels $|1\rangle$ and $|2\rangle$); Δ_1 represents the detuning of the excitation laser; Γ_1 represents spontaneous decay rate of the excitation state; Ω_2 denotes the Rabi frequency of the UV laser (coupling Levels $|1\rangle$ and $|3\rangle$); and Δ_2 represents the UV laser detuning, Γ_2 represents spontaneous decay rate of the Rydberg state $|3\rangle$.

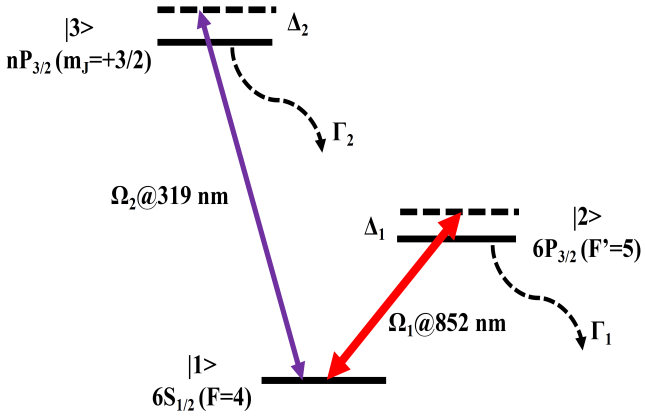

Figure 1. Schematic diagram of the V-type three level system of Cs atoms. State $|1\rangle$ ($6S_{1/2}$ (F=4)) and state $|2\rangle$ ($6P_{3/2}$ ($F^{'}$=5)) are coupled by a infrared laser (Ω_1@852 nm) with detuning Δ_1 and spontaneous decay rate Γ_1. Simultaneously, the UV laser (Ω_2@319 nm) excites Cs atoms from state $|1\rangle$ to state $|3\rangle$ ($nP_{3/2}$ (m_J=+3/2)) with corresponding detuning Δ_2 and spontaneous decay rate Γ_2. Dashed arrows indicate radiation decay channels, while solid arrows represent laser coupling pathways.

In order to explain the dynamics of the interaction between light and atoms in a V-type three-level system, we consider the following theory,

$$H = \frac{\hbar}{2}\begin{pmatrix} 0 & \Omega_1 & \Omega_2 \\ \Omega_1 & -2\Delta_1 & 0 \\ \Omega_2 & 0 & -2\Delta_2 \end{pmatrix} \tag{1}$$

$$\rho = \begin{pmatrix} \rho_{11} & \rho_{12} & \rho_{13} \\ \rho_{21} & \rho_{22} & \rho_{23} \\ \rho_{31} & \rho_{32} & \rho_{33} \end{pmatrix} \tag{2}$$

$$L(\rho) = \begin{pmatrix} \gamma_2\rho_{22} + \gamma_3\rho_{33} & -\frac{1}{2}\gamma_2\rho_{12} & -\frac{1}{2}\gamma_3\rho_{13} \\ -\frac{1}{2}\gamma_2\rho_{21} & -\gamma_2\rho_{22} & -\frac{1}{2}(\gamma_2+\gamma_3)\rho_{23} \\ -\frac{1}{2}\gamma_3\rho_{31} & -\frac{1}{2}(\gamma_2+\gamma_3)\rho_{32} & -\gamma_3\rho_{33} \end{pmatrix} \tag{3}$$

$$\dot{\rho} = -\frac{i}{\hbar}[H,\rho] + L(\rho) \tag{4}$$

Here H represents the Hamiltonian describing the interaction of the V-type three-energy-level atoms with the laser field; $\rho_{ij}(i,j=1,2,3)$ denotes the elements of the density matrix. When $i=j$, ρ_{ii} represents the diagonal elements of the density matrix, corresponding to the atomic population probabilities of each energy level. Conversely, when $i \neq j$, ρ_{ij} describes the non-diagonal elements, characterizing the coherence between two energy levels. $L(\rho)$ represents the decoherence matrix, which accounts for the dissipation processes within the system. γ_2 represents the spontaneous radiation decay rate of the cesium atom $6P_{3/2}$; while γ_3 denotes the spontaneous radiation decay rate of the cesium atom Rydberg state $nP_{3/2}$.

The TLFS[16,17,21,25] serves as a powerful tool to characterize the dynamic process of cold-atom fluorescence attenuation induced by Rydberg excitation within a MOT. In this context, cold-atom fluorescence arises from the spontaneous radiation of the excited state, rendering it directly proportional to the atomic population probability of the excited state. Utilizing Eq. (1–4), we derive the instantaneous steady-state solution, incorporating the temporal density matrix, to analyze the population probability ρ_{22} of energy level 2.

As depicted in Fig. 2, the excitation laser Rabi frequency Ω_1, and the UV laser Rabi frequency Ω_2 are held constant, while the UV laser detuning, and scan the UV laser detuning Δ_2 is scanned to generate the double-peak spectral structure. Since the vertical axis represents the atomic population probability of excited state 2, which is directly proportional to the fluorescence intensity of the cold atoms, this simulation effectively characterizes the physical behavior of cold atoms in a MOT with reduced fluorescence due to Rydberg excitation. In this spectrum, Peaks 1 and 2 correspond to the double peaks of the AT doublet. These peaks exhibit increased symmetry as the excitation laser detuning approaches resonance, while the interval between the peaks expands with increasing excitation laser detuning.

Trap-loss fluorescence spectroscopy and AT doublet in Cs MOT

As illustrated in Fig. 3, the image on the left shows the atomic energy level diagram of the MOT and the single-step Rydberg excitation. The thick red arrow represents the cooling laser beam, and its Rabi frequency is marked Ω_1, and the detuning is Δ_1; The thin red arrow represents the repumping laser beam, which is used to pump the atoms populated on $6S_{1/2}$ (F=3) to continue to participate in the cooling process; The purple arrow represents the UV laser beam for single-step Rydberg excitation, with a Rabi frequency labeled Ω_2 and a detuned as Δ_2. The above marks correspond one-to-one to Fig. 1 in the theoretical part, however, where we ignore the behavior that the atoms will populate in $6S_{1/2}$ (F=3), i.e., the repumping laser is not considered. And, in the Fig.3 (b), the Cs MOT is housed within a $30 \times 30 \times 120$ mm^3 ultra-high vacuum (UHV) glass cell, with typical pressure of approximately 1×10^{-9} Torr. The frequency of the cooling laser beam, which has a Gaussian diameter of approximately 10 mm, is locked to the Cs $6S_{1/2}$ (F=4) $\rightarrow$ $6P_{3/2}$ (F$'$=5) cycling transition with a detuning Δ_1. The repumping laser beam, with a Gaussian diameter of around 9 mm, is resonant with the Cs $6S_{1/2}$ (F=3) $\rightarrow$ $6P_{3/2}$ (F$'$=4) transition. The cooling laser beam and repumping laser beams are combined and then are divided into three parts: one part along the Z and -Z directions, accounting for approximately 40% of the power. The remaining two parts are split equally in power and directed in the XY plane at an angle of about 80°. A gradient magnetic field is produced by a pair of anti-Helmholtz coils driven by a constant-current source, generating a typical axial magnetic field gradient of 10 Gauss/cm with a current of 9 A. Consequently, a bright cloud of cold atomic ensemble can be immediately observed using a CCD camera.

Since a MOT cannot trap Rydberg atoms, Rydberg atoms are lost when the UV laser[26–29] couples Cs atoms from the $6S_{1/2}$ (F=4) to the $nP_{3/2}$ (m_J=+3/2) state, achieving single-step Rydberg excitation. In other words, the excitation of Rydberg atoms can be inferred by observing the trap-loss fluorescence from a cold cloud in the MOT.

During the experiment, the change in frequency of our UV laser system is achieved by scanning it point by point. Each frequency point lasts for 30 s. The CCD camera is triggered for taking the photograph of the cold atom within 30 s, the timestamp of the initial trigger is synchronized, which occurs 5 s after the UV laser is adjusted to the target frequency, and taking the photograph ends at the next time the UV laser frequency is modified, the exposure time of the CCD camera is 5 ms, and the CCD's trigger frequency is 0.2 Hz. In a spectrum acquisition process, each frequency point lasts for 30 s, and the

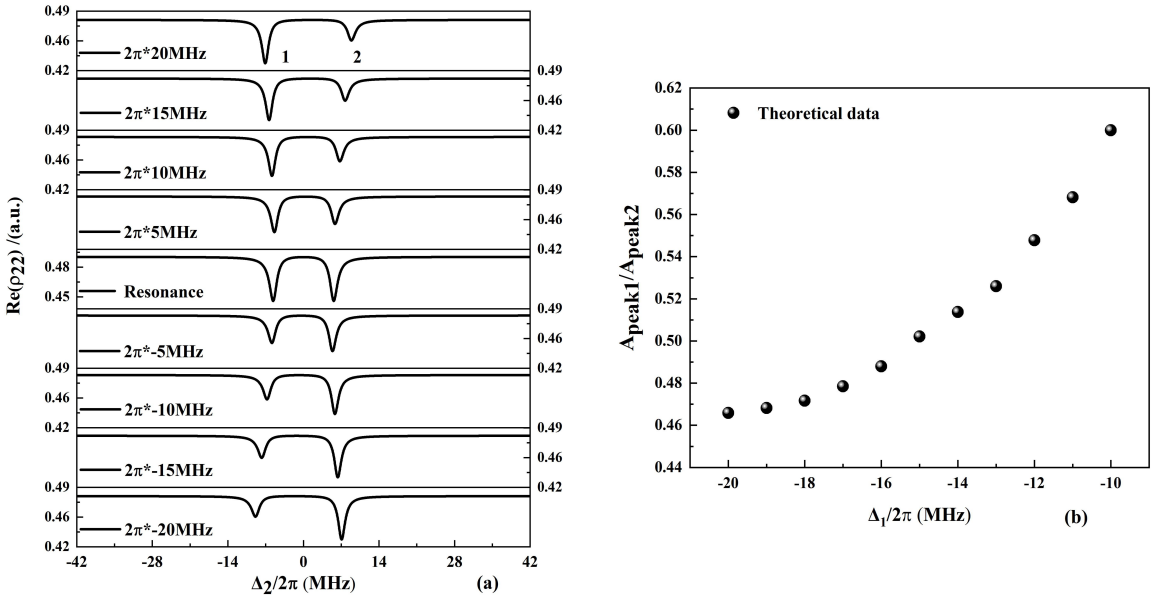

Figure 2. (a), according to Eq. (1-4), simulations are carried out to obtain the relationship between Re(ρ_{22}) and the UV laser detuning Δ_2, which exhibits an obvious AT bimodal structure; and the detuning of the excitation laser Δ_1 is constantly changed. When the detuning is gradually reduced, the AT doubleT tend to be symmetric gradually. (b), for the purpose of our actual experiments (the cooling laser frequency to maintain the normal operation of the MOT should be negatively detuned), it is taken as -20 MHz to -10 MHz, and the ratio of their respective corresponding double-peaks amplitudes. The black squares are simulated data points.

UV laser frequency needs to be changed about 45∼55 times, covering about 175∼200 MHz, with a total duration of about 30 minutes.

Since the UV Rabi frequency is the order of several hundred kHz, the Rydberg excitation time is must less than the CCD exposure time. Therefore, we believe that the loss of atomic number in the MOT is completely at a steady state within the 5 ms time window. Within 30 s, five fluorescence images of cold atoms will be obtained, and three of them will be randomly selected to calibrate the remaining proportion of cold atoms in the MOT at the current UV laser frequency. For every five data acquisitions, we will take pictures of the MOT that are not Rydberg excited by UV laser for image processing and fluorescence intensity normalization for these five data acquisitions. After a spectral data acquisition, we use a MATLAB program to process the fluorescence images of cold atoms, and the relative fluorescence intensity is calculated by dividing the total fluorescence intensity of the cold atoms in the MOT with UV laser excitation by the reference fluorescence intensity without UV laser excitation. In addition, background light was subtracted to correct for the effect of background scattered light.

Throughout the experiment, we utilize a wavelength meter (HighFinesse, WS-7) to monitor the red light frequency in real time, ensuring the accuracy of the UV frequency. Additionally, the wave meter is calibrated after every five acquisitions using the probe beam ($6S_{1/2}$ (F=4) $\rightarrow$ $6P_{3/2}$ (F$'$=5), 351.72196 THz[30]) as the frequency reference.

We select $71P_{3/2}$ as the target Rydberg state, experimentally observe the TLFS and its AT doublet, and investigat the dependence of AT doublet characteristics on laser detuning. Specific results are given in[7,17] In this paper, we only analyze the symmetry and interval of the AT doublet of the TLFS. As shown in Fig. 4, we fixed the Rabi frequency Ω_1 of the cooling laser beam to $2\pi \times 8.1$ MHz and the UV laser Rabi frequency Ω_2 to $2\pi \times 117$ kHz, and gradually decreased the cooling laser detuning Δ_1 ((top): -15 MHz; (middle): -12 MHz; (bottom): -10 MHz), and obtained three sets of spectroscopy. The ratio of the amplitudes of the AT doublet (peaks 1 and 2) gradually increases with the decrease of the cooling laser detuning, i.e., the double-peaks gradually tend to be symmetric; and according to $\tilde{\Omega} = \sqrt{\Omega_1^2 + \Delta_1^2}$, the intervals of the AT doublet gradually decrease with the decrease of the detuning.

However, to our surprise, the full width at half maximum (FWHM) of the TLFS measured at four different principal quantum numbers was all on the order of 20 MHz. We propose five possible mechanisms for the linewidth broadening of the TLFS:

Firstly, the Rabi frequency of the cooling laser is still at a relatively high order of magnitude, which still causes the ground state is broadened by a factor of 1.7 due to power broadening. Secondly, The Zeeman broadening in the z-direction at the center

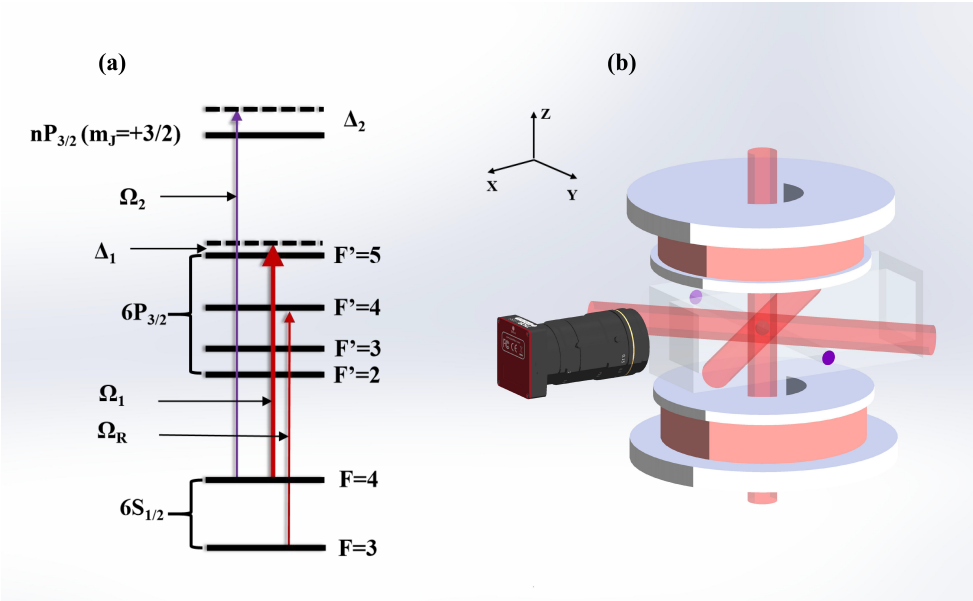

Figure 3. Diagram of Cs relevant energy level and MOT setup. (a) displays the atomic energy level diagram, emphasizing the cooling laser beam (thick red arrows) and repumping laser beam (thin red arrows) and UV laser beam (purple arrows) for single-step Rydberg excitation. (b) presents the experimental configuration, featuring the trapping region surrounded by a pair of coils generating a quadrupole magnetic field and the intersection of laser beams for cooling. The imaging system, aligned along a principal axis, enables precise monitoring of atomic fluorescence.

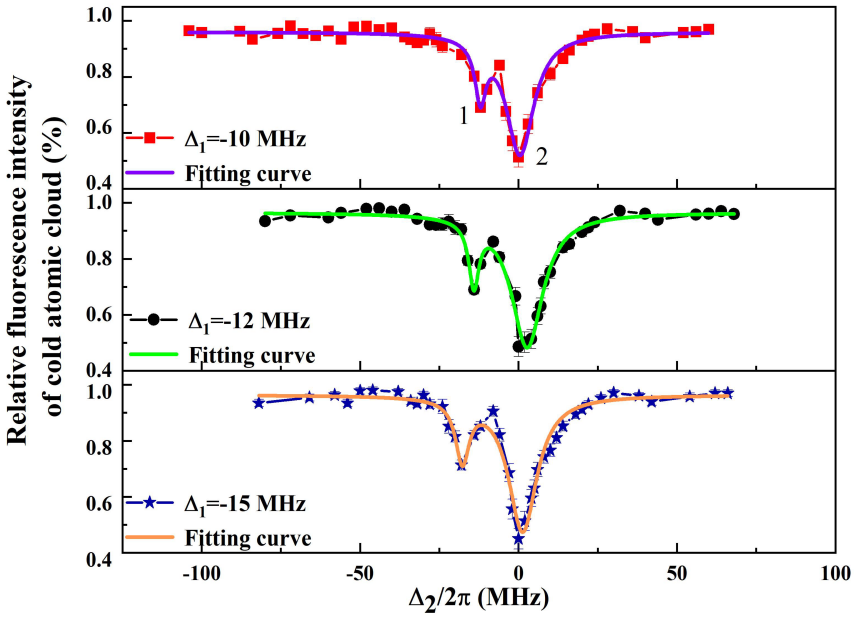

Figure 4. The TLFS and their AT doublet at different amounts of cooling laser detuning. By adjusting the parameters, a significant change in the resonance signal can be observed. Among them, the cooling laser Rabi frequency is fixed to $2\pi \times 8.1$ MHz, and the Rabi frequency of UV laser is $2\pi \times 117$ kHz, and the detuning of cooling laser is gradually reduced, and three sets of spectral signals ((top): -10 MHz; (Medium): -12 MHz; (bottom): -15 MHz). The amplitude ratio of peaks 1 and 2 gradually increases, tends to be asymmetrical, and the AT doublet interval also increases gradually with the increase of cooling laser detuning. The red squares, black circles, and blue stars are experimental data, and the purple, green, and orange curves are multi-peaks Lorentzian profile fitting curves.

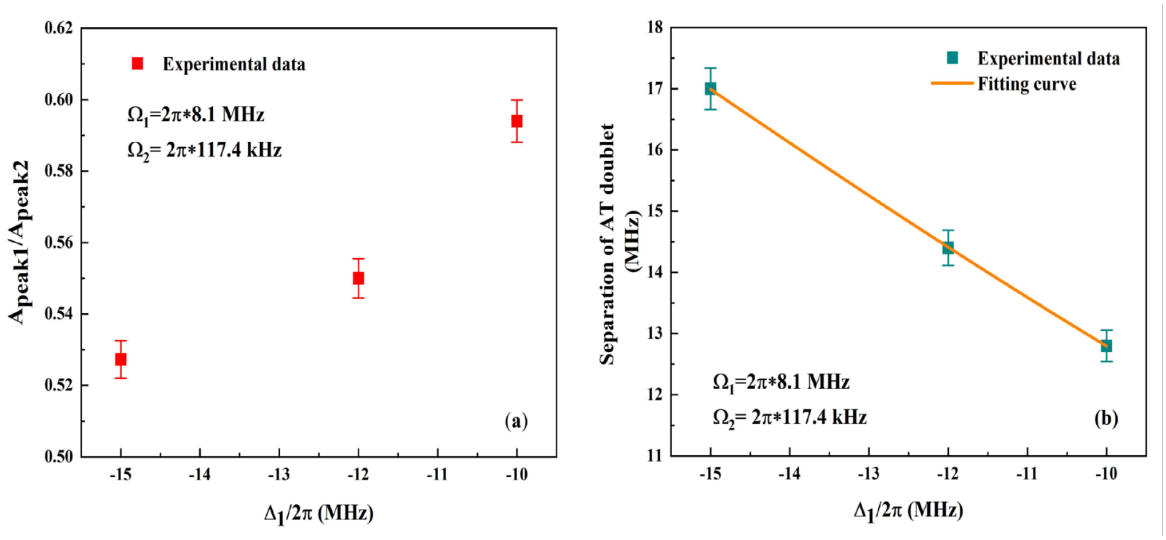

Figure 5. Comparative analysis of experimental results obtained under varying conditions. (a) The red data points illustrate the trend of the bimodal amplitude ratio as a function of the cooling laser detuning, with uncertainties indicated by error bars. (b) The green data points represent the AT doublet interval, while the nonlinear dependence predicted by the theoretical model is highlighted through the orange solid line fitting.

of the MOT can be calculated according to $\Delta\Gamma = \frac{\mu_B}{h} g_J(S_{1/2}) \frac{\partial B}{\partial z} \Delta z$. The ground state $6S_{1/2}$ broadens to 0.96 MHz due to the presence of a magnetic field. Thirdly, our atoms are exposed to severe blackbody radiation (BBR) at room temperature that will directly couple the target Rydberg state with the adjacent Rydberg state. So, the lifetime of the target Rydberg state decreases dramatically, and the typical Rydberg state lifetime is about 10 μs, and the width of the Rydberg state energy level is broadened to 100 kHz. Fourth, as can be seen in Fig. 5, the baseline is less than 100% at the UV laser separation resonance position, there is still a 15% $\sim$ 20% loss of cold atomic fluorescence intensity. This is due to the fact that the cold atoms in the magneto-optical trap are constantly affected by ionization, and we speculate that the mechanisms that lead to ionization are photoionization, field ionization, and collision ionization. Due to the presence of ionization, the overall spectral signal increases by 15% $\sim$ 20%, then we can simply infer that the spectral linewidth is broadened by at least 15% due to the presence of ionization. Last, due to the existence of the ionization mechanism, a cold plasma is formed near the cold atoms, which in turn generates a local electric field of a certain intensity, whose electric field intensity is space-dependent. When such a local electric field is superimposed with the background DC electric field, the Stark shift formed on the Rydberg state will be spatially dependent. It can be roughly inferred that the remaining broadening of about 5 MHz comes from the local electric field generated by the cold plasma[31].

Extend sparse data using RNN

To address the challenge of data sparsity in theoretical modeling, we propose a reverse neural network (RNN) approach to generate high-density datasets and optimize the analysis accuracy of AT doublet characteristics, as show in Fig.6. By inferring experimental condition parameters from target outputs, RNN robustly constructs high-density experimental datasets and effectively captures nonlinear characteristics in complex systems. The network architecture consists of two hidden layers, each with 128 neurons, utilizing Rectified Linear Unit (ReLU) activation functions to handle nonlinearity, and a linear activation function in the output layer to produce continuous feature data. The model training is based on sparse experimental data, combined with predictions from the forward neural network.

In the RNN model proposed in this work, a systematic optimization of hyperparameters was conducted to ensure model stability and prediction accuracy. Firstly, the learning rate was initialized to 0.001 and dynamically adjusted using the Adam optimizer to accelerate convergence while avoiding local optima. To prevent overfitting, L_2 regularization was applied with a coefficient of 0.01 to constrain excessive weight growth. Additionally, Dropout was utilized in the hidden layers, randomly deactivating 20% of the neurons to enhance the model's generalization capability. The Rectified Linear Unit (ReLU) activation function was chosen for the hidden layers to improve the processing of nonlinear characteristics, while a linear activation function was used in the output layer to generate continuous predictions.

During hyperparameter optimization, the optimal parameter combination was selected through cross-validation, with Mean Squared Error (MSE) serving as the loss function. On the validation set, the optimized model exhibited stable convergence, with fluctuations in the validation curve kept below 1%. Furthermore, the final validation set MSE decreased significantly from

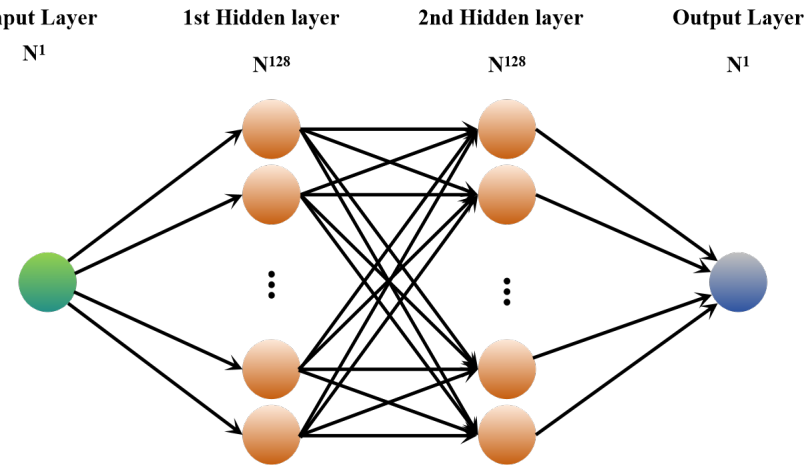

Figure 6. The schematic representation of the neural network depicts an architecture comprising an input layer, two hidden layers, and an output layer. Each hidden layer contains 128 neurons, processed through a nonlinear activation function, enabling the model to effectively learn and represent intricate patterns and relationships within the data. The layers are fully connected, facilitating comprehensive learning of feature interactions and ensuring that the network can capture the complex dependencies inherent in the input data.

an initial value of 0.045 to 0.023, demonstrating notable improvement. These optimization steps ensured the reliability of the model in expanding sparse data and capturing nonlinear characteristics, providing robust support for subsequent experimental analysis.

Upon completion of training, the RNN predicts the corresponding cooling laser detuning based on the input AT doublet amplitude ratio and, using the forward neural network, generates a dense spectral dataset. The generated dense dataset not only mitigates the limitations imposed by sparse experimental conditions but also markedly enhances the model's accuracy in fitting the relationship between cooling laser detuning and AT doublet characteristics. The application of the dense dataset validates the influence of cooling laser detuning on symmetry and interval, offering a novel research tool and methodological framework for optimizing multi-parameter configurations in complex systems.

Figure 7 presents a detailed comparison of experimental data, theoretical models, and neural network training results, while also assessing the neural network's performance in nonlinear data fitting through the analysis of loss curves. The four subfigures collectively offer a comprehensive evaluation of the neural network's accuracy, stability, and its ability to capture the physical significance inherent in modeling complex physical processes.

In Fig. 7(a), the horizontal axis represents the cooling laser detuning, while the vertical axis denotes the normalized peak ratio. The plot visualizes the experimental data (red triangular markers with error bars), the theoretical model (yellow squares), and the dense dataset predicted by the neural network (purple circles). The RNN effectively transforms the discrete and sparse experimental data points into a dense dataset that aligns closely with the theoretical model. This demonstrates the neural network's capability to accurately characterize nonlinear dynamical behaviors in complex physical processes, reinforcing the consistency between the experimental data and the theoretical model. The corresponding Fig. 7(b) depicts the trends in training and validation losses, with the number of training epochs on the horizontal axis and the loss values on the vertical axis. The main plot reveals a rapid decline in loss during the initial training phase, followed by a plateau, signifying the successful convergence of the model. The inset graph magnifies the loss trends during the later training stages, illustrating that both training and validation losses stabilize at low levels, thereby confirming the model's robust generalization capability and the absence of overfitting or underfitting.

Figure 7(c) illustrates the variation of AT bimodal separation as a function of detuning, where the horizontal axis represents detuning and the vertical axis denotes the AT bimodal separation interval. A comparison among the experimental data (red markers with error bars), the dense data predicted by the neural network (blue markers), and the theoretical fitting curve (orange line) demonstrates that the neural network precisely captures the nonlinear variation pattern of AT bimodal separations. The dense predicted dataset exhibits strong consistency with both the experimental points and the theoretical model. Fig. 7(d) evaluates the loss curves associated with the fitted training process for the AT doublet interval, analogous to Fig. 7(b), illustrating the progression of training and validation losses over the training epochs. Both the main plot and the inset highlight the model's rapid convergence during the initial training stages, followed by stabilization of the loss values. Minor fluctuations observed in the validation loss further underscore the model's robust training stability and strong generalization capability.

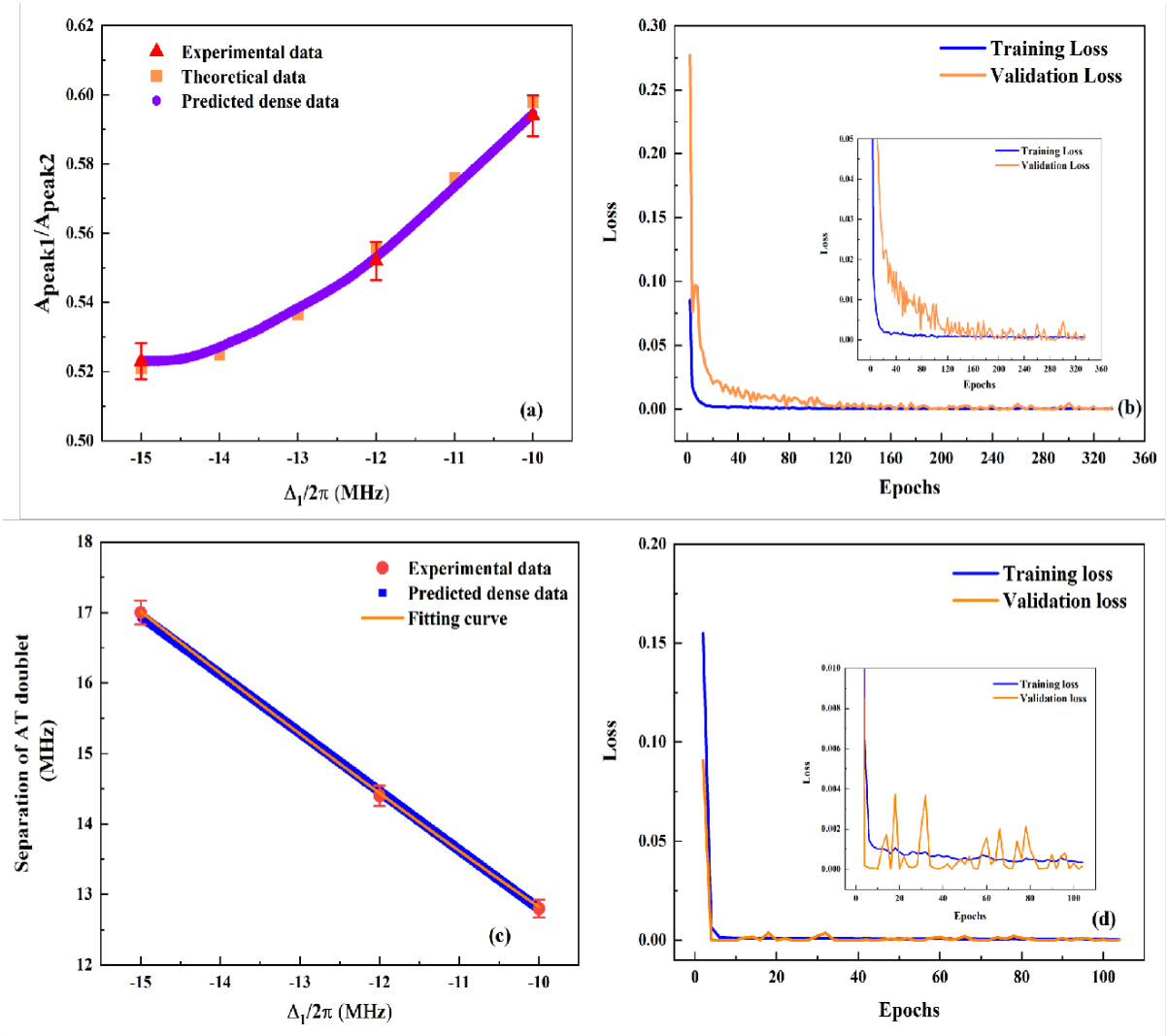

Figure 7. Comprehensive comparative analysis of experimental data, theoretical models, and predictions from the inverse neural network, accompanied by the trends observed in training and validation losses. (a) Normalized peak ratio: the reverse neural network efficiently generates a dense dataset that closely aligns with both experimental data and theoretical models, effectively capturing and accurately characterizing the nonlinear properties. (b) Loss curves for the normalized peak ratios illustrate the model's stable convergence and robust generalization capability. (c) For AT doublet intervals, the neural network accurately predicts nonlinear variation patterns, with the dense datasets it generates exhibiting strong concordance with experimental data and theoretical models, thereby preserving a high level of consistency. (d) Loss curves further confirm the stability of the model's training process and its adherence to physical principles, emphasizing the reliability of its predictions.

We have effectively addressed the limitations of sparse data in modeling and analysis in cold atom experiments using RNN. By employing RNN, sparse experimental data is expanded into a high-density virtual dataset, significantly improving the fitting accuracy of theoretical models and providing additional support for studying nonlinear details in spectral characteristics. Compared to traditional methods that rely directly on sparse data, integrating RNN-generated high-density data enables more precise capture of the complex variation trends in AT doublet characteristics, verifying the model's broad applicability under different experimental conditions.

Conclusions

This study effectively addresses the challenges posed by experimental data sparsity and nonlinear fitting through the introduction of a reverse neural network (RNN), offering a novel methodology to investigate AT doublet of the TLFS in Cs MOT with single-step Rydberg excitation using a 319-nm UV laser. The dense dataset generated by the RNN markedly enhances the accuracy of data fitting, enabling the resolution of the effects of cooling laser detuning on the symmetry and intervals of AT doublet. The results reveal that the symmetry of AT doublet gradually converges as the cooling laser detuning decreases, while the doublet interval exhibits a nonlinear decrease. Compared to traditional methods, the RNN demonstrates exceptional nonlinear modeling capabilities, offering reliable technical support for the multi-parameter optimization of complex experimental systems.

Additionally, the stability and generalization capability of the neural network model in dense data scaling are validated through an evaluation of its training and validation loss curves. This study not only highlights the innovative application of RNN in spectroscopy but also paves the way for the broader use of machine learning techniques in addressing challenges within nonlinear physical systems. Furthermore, it provides a valuable technical reference for advancing future research in quantum optics and cold atomic physics.

However, the performance of RNN is heavily influenced by the quality of the input experimental data. When experimental data are affected by random noise or systematic errors, the generated dense datasets may exhibit significant deviations, thereby restricting their direct applicability under complex experimental conditions. Moreover, this study primarily investigates the impact of a single parameter (detuning) on AT doublet, while the exploration of high-dimensional parameter spaces (e.g., Rabi frequency of multiple lasers versus detuning) warrants further extension. Future research could focus on optimizing the RNN architecture and incorporating advanced denoising techniques to enhance the model's robustness against experimental noise. Simultaneously, extending the joint analysis to multi-parameter dimensions would enable its application to more complex experimental scenarios. Incorporating physical constraints into model training is anticipated to significantly enhance the applicability and reliability of RNN in modeling complex spectral systems.

References

1. T. F. Gallagher, "Rydberg atoms," Cambridge University Press, 2005.
2. A. Browaeys and T. Lahaye, "Many-body physics with individually controlled Rydberg atoms," *Nature Physics*, vol. 16, no. 2, p. 132–142, 2020.
3. C. S. Adams, J. D. Pritchard, and J. P. Shaffer, "Rydberg atom quantum technologies," *Journal of Physics B: Atomic, Molecular and Optical Physics*, vol. 53, no. 1, 012002, 2019.
4. M. Saffman, T. G. Walker, and K. Mølmer, "Quantum information with Rydberg atoms," *Reviews of Modern Physics*, vol. 82, no. 3, 2313, 2010.
5. A. Arias, G. Lochead, T. M. Wintermantel, S. Helmrich, and S. Whitlock, "Realization of a Rydberg-dressed Ramsey interferometer and electrometer," *Physical Review Letters*, vol. 122, no. 5, 053601, 2019.
6. M. Y. Jing, Y. Hu, J. Ma, H. Zhang, L. J. Zhang, L. T. Xiao, and S. T. Jia, "Atomic superheterodyne receiver based on microwave-dressed Rydberg spectroscopy," *Nature Physics*, vol. 16, no. 9, p. 911–915, 2020.
7. J. D. Bai, S. Liu, J. Y. Wang, J. He, and J. M. Wang, "Single-photon Rydberg excitation and trap-loss spectroscopy of cold cesium atoms in a magneto-optical trap by using of a 319-nm ultraviolet laser system," *IEEE Journal of Selected Topics in Quantum Electronics*, vol. 26, 1600106, 2020.
8. D. A. Anderson, S. A. Miller, G. Raithel, J. A. Gordon, M. L. Butler, and C. L. Holloway, "Optical measurements of strong microwave fields with Rydberg atoms in a vapor cell," *Physical Review Applied*, vol. 5, no. 3, 034003, 2016.
9. S. Kumar, H. q. Fan, H. Kübler, A. J. Jahangiri, and J. P. Shaffer, "Rydberg-atom based radio-frequency electrometry using frequency modulation spectroscopy in room temperature vapor cells," *Optics Express*, vol. 25, no. 8, p. 8625–8637, 2017.
10. M. Boninsegni, H. q. Prokof'ev, "Colloquium: supersolids: what and where are they?," *Reviews of Modern Physics*, vol. 84, 759, 2012.

11. A. W Glaetzle, M. Dalmonte, R. Nath, C. Gross, I. Bloch, P. Zoller, "Designing frustrated quantum magnets with laser dressed Rydberg atoms," *Physical Review Letters*, vol. 114, 173002, 2015.

12. L. I. R. Gil, R. Mukherjee, E. M. Bridge, M. P. A. Jones, T. Pohl, "Spin squeezing in a Rydberg lattice clock," *Physical Review Letters*, vol. 112, 103601, 2014.

13. J. Lee, M. J. Martin, Y. Y. Jau, T. Keating, T.H. Deutsch, G. W. Biedermann, "Demonstration of the Jaynes–Cummings ladder with Rydberg-dressed atoms," *Physical Review A*, vol. 95, 041801(R), 2017.

14. Y. Y. Jau, A. M. Hankin, T. Keating, T.H. Deutsch, G. W. Biedermann, "Entangling atomic spins with a Rydberg-dressed spin-flip blockade," *Nature Physics*, vol. 12, p. 71–74, 2016.

15. S. h. Aulter, C. h. Townes, "Stark effect in rapidly varying fields," *Physical Review*, vol. 100, no. 2, p. 703–723, 1955.

16. J. D. Bai, J. Y. Wang, S. Liu, J. He, and J. M. Wang, "Autler–Townes doublet in single-photon Rydberg spectra of cesium atomic vapor with a 319 nm UV laser," *Applied Physics B*, vol. 125, no. 3, 33, 2019.

17. X. Wang, X. K. Hou, F. F. Lu, R. Chang, L. L. Hao, W. J. Su, J. D. Bai, J. He, and J. M. Wang, "Autler–townes doublet in the trap-loss fluorescence spectroscopy due to single-step direct Rydberg excitation of cesium cold atomic ensemble," *AIP Advances*, vol. 13, no. 3, 035126, 2023.

18. D. A. Braje, V. Balić, S. Goda, G. Y. Yin, S. E. Harris, "Frequency mixing using electromagnetically induced transparency in cold atoms," *Physical Review Letter*, vol. 93, 183601, 2004.

19. L. V. Hau, S. E. Harris, Z. Dutton, C. H. Behroozi, "Light speed reduction to 17 meters per second in an ultracold atomic gas," *Nature*, vol. 397, p. 594-598, 1999.

20. U. Raitzsch, R. Heidemann, H. Weimer, B. Butscher, P. Kollmann, R. Löw, H. P. Büchler, T. Pfau, "Investigation of dephasing rates in an interacting Rydberg gas," *New Journal of Physics*, vol. 11, 055014, 2009.

21. Y. F. Cao, W. G. Yang, H. Zhang, M. Y. Jing, W. B. Li, L. J. Zhang, L. T. Xiao, and S. T. Jia, "Dephasing effect of Rydberg states on trap loss spectroscopy of cold atoms," *Journal of the Optical Society of America B*, vol. 39, no. 8, p. 2032–2036, 2022.

22. E. H. Ahmed, S. Ingram, T. Kirova, O. Salihoglu, J. Huennekens, J. Qi, Y. Guan, A. M. Lyyra, "Quantum control of the spin-orbit interaction using the Autler-Townes effect," *Physical Review Letters*, vol. 107, 163601, 2011.

23. L. Phuttitarn, M. Becker, R. Chinnarasu, M. Graham, M. Saffman, "Enhanced measurement of neutral-atom qubits with machine learning," *Physical Review Applied*, vol. 22, 024011, 2024.

24. X. Meng, Y. W. Zhang, X. C. Zhang, S. C. Jin, T. R. Wang, L. Jiang, L. T. Xiao, S. T. Jia, Y. H. Xiao, "Machine learning assisted vector atomic magnetometry," *Nature Communications*, vol. 14, 6105, 2023.

25. C. Halter, A. Miethke, C. Sillus, A. Hegde, and A. Göerlitz, "Trap-loss spectroscopy of Rydberg states in ytterbium," *Journal of Physics B : Atomic, Molecular and Optical Physics*, vol. 56, 055001, 2023.

26. J. Y. Wang, J. D. Bai, J. He, and J. M. Wang, "Realization and characterization of single-frequency tunable 637.2 nm high-power laser," *Optics Communications*, vol. 370, p. 150–155, 2016.

27. J. Y. Wang, J. D. Bai, J. He, and J. M. Wang, "Development and characterization of a 2.2 W narrow-linewidth 318.6 nm ultraviolet laser," *Journal of the Optical Society of America B*, vol. 33, no. 10, p. 2020–2025, 2016.

28. J. D. Bai, J. Y. Wang, J. He, and J. M. Wang, "Electronic sideband locking of a broadly tunable 318.6 nm ultraviolet laser to an ultra-stable optical cavity," *Journal of Optics*, vol. 19, 045501, 2017.

29. J. M. Wang, J. D. Bai, J. Y. Wang, S. Liu, B. D. Yang, and J. He, "Realization of a watt-level 319-nm single-frequency cw ultraviolet laser and its application in single-photon Rydberg excitation of cesium atoms [invited]," *Chinese Optics*, vol. 12, no. 4, p. 701–718, 2019 (in Chinese).

30. A. Kramida, Yu. Ralchenko, J. Reader, (NIST ASD Team) (2024), "NIST Atomic Spectra Database (version 5.12)," Available: https://physics.nist.gov/asd [Nov 12 2024].

31. M. P. Robinson, B. L. Tolra, M. W. Noel, T. F. Gallagher, and P. Pillet, "Spontaneous evolution of Rydberg atoms into an ultracold plasma," *Physical Review Letters*, vol. 85, no. 21, p. 4466–4469, 2000.

Acknowledgements

This work is partially supported by the National Key R & D Program of China (2021YFA1402002), the National Natural Science Foundation of China (12474483), and the Fundamental Research Program of Shanxi Province (202403021211013).

Author contributions statement

X.K.H. and J.M.W. conceived the experimental concept; All contributed to the design, and X.K.H. and Y.W.W. conducted the experiment; X.K.H. and J.M.W. analyzed the data and X.K.H., J.H. and J.M.W. wrote the paper; J. M. W. supervised the research project.

Additional information

Competing financial interests: The authors declare no competing financial interests.